

PAPER • OPEN ACCESS

# Towards bi-magnetic nanocomposites as permanent magnets through the optimization of the synthesis and magnetic properties of $\text{SrFe}_{12}\text{O}_{19}$ nanocrystallites

Recent citations

- [On Modeling of Synthesis Process of Boron Carbide Based Nanocomposites](#)  
Levan Chkhartishvili *et al*

To cite this article: Pierfrancesco Maltoni *et al* 2021 *J. Phys. D: Appl. Phys.* **54** 124004

View the [article online](#) for updates and enhancements.



**IOP | ebooks™**

Bringing together innovative digital publishing with leading authors from the global scientific community.

Start exploring the collection—download the first chapter of every title for free.

# Towards bi-magnetic nanocomposites as permanent magnets through the optimization of the synthesis and magnetic properties of SrFe<sub>12</sub>O<sub>19</sub> nanocrystallites

Pierfrancesco Maltoni<sup>1</sup> , Tapati Sarkar<sup>1</sup> , Gaspare Varvaro<sup>2</sup> , Gianni Barucca<sup>3</sup> , Sergey A Ivanov<sup>1,4</sup>, Davide Peddis<sup>2,5</sup>  and Roland Mathieu<sup>1</sup> 

<sup>1</sup> Department of Materials Science and Engineering, Uppsala University, Box 35, SE-751 03 Uppsala, Sweden

<sup>2</sup> Istituto di Struttura della Materia-CNR, 00015 Monterotondo Scalo (RM), Italy

<sup>3</sup> Department SIMAU, University Politecnica delle Marche, Via Brecce Bianche, Ancona, Italy

<sup>4</sup> Department of Chemistry, M.V. Lomonosov Moscow State University, Leninskie Gory 1/3, Moscow 119991, Russia

<sup>5</sup> Dipartimento di Chimica e Chimica Industriale, Università degli Studi di Genova, Via Dodecaneso 31, I-16146 Genova, Italy

E-mail: [pierfrancesco.maltoni@angstrom.uu.se](mailto:pierfrancesco.maltoni@angstrom.uu.se), [davide.peddis@unige.it](mailto:davide.peddis@unige.it) and [roland.mathieu@angstrom.uu.se](mailto:roland.mathieu@angstrom.uu.se)

Received 3 September 2020, revised 24 November 2020

Accepted for publication 9 December 2020

Published 20 January 2021



CrossMark

## Abstract

Sol–gel synthesis was used in order to obtain nanocrystallites of the SrFe<sub>12</sub>O<sub>19</sub> (SFO) hexaferrite in an efficient and reliable way. By optimizing the initial synthetic conditions, we were able to control the size of the nanoparticles (NPs), at lower annealing temperature. The x-ray powder diffraction, transmission electron microscopy (TEM), and magnetic measurements have demonstrated a significant relation between the morphology, size, and magnetic properties of the nanoscale SFO, revealing a definite dependence on the crystallite size along the *c*-axis. The obtained NPs appear almost isotropic, in the form of platelets and exhibit similar magnetic performance, in terms of the energy product (BH)<sub>MAX</sub>, thus, demonstrating the suitability of reducing the annealing temperature without any deterioration in the magnetic properties. Additionally, this work illustrates the feasibility of the sol–gel bottom-up approach to employ magnetic NPs as building-blocks for designing hard/soft exchange-coupled bi-magnetic nanocomposites, combining the high coercivity of a hard phase (SFO) and the high saturation magnetization of a soft phase (CoFe<sub>2</sub>O<sub>4</sub>); in this regard, we discuss the tunability of the magnetic anisotropy by symbiotically restricting the growth of both phases.



Original content from this work may be used under the terms of the [Creative Commons Attribution 4.0 licence](https://creativecommons.org/licenses/by/4.0/). Any further distribution of this work must maintain attribution to the author(s) and the title of the work, journal citation and DOI.

Supplementary material for this article is available [online](#)

Keywords: ferrites, nanocomposites, permanent magnets, sol–gel chemistry

(Some figures may appear in colour only in the online journal)

## 1. Introduction

Magnetic nanoparticles (NPs) have gained increasing attention owing to their potential use as building blocks for next-generation permanent magnets [1, 2]. Conventionally, permanent magnets are based on intermetallic compounds containing rare-earths (RE) metals (such as Nd, Sm, Dy, Tb, and 3d metals) and are used in virtually every aspect of modern life. They are the main building blocks of motors and generators used in electric energy generation and conversion, including novel environment-friendly technologies related to electric cars, wind turbines, hydropower, and magnetocaloric refrigeration [3]. The transition from fossil to sustainable energy thus implies an ever-increasing demand for permanent magnets. To date, RE-based permanent magnets (i.e. Nd–Fe–B and Sm–Co alloys) are the best performing materials; they cover 65% of the market. The second family of magnets produced at large scale is the magnetically hard hexaferrites (e.g. BaM and SrM;  $M = \text{Fe}_{12}\text{O}_{19}$ ), characterized by a smaller maximum energy product, that provide another 34% of the total market [2, 4]. Nowadays, the supply of REs is a critical issue for the permanent magnet industry. The extremely low number of extraction sites, combined with the continuous growth in demand, makes the RE elements extremely vulnerable to price fluctuations and shortages, thus increasing the interest in low cost hexaferrites. Such a scenario has stimulated an intense activity for the search of new nanomaterials with a reduced or even zero content of REs to bridge the gap between hexaferrites and RE permanent magnets [3]. While a major achievement would be to find new phases (e.g. MnAl, MnBi, Fe–N, Co–Hf, etc) [3], much can be done to improve the performance of known materials. Despite metallurgical processes have been continuously improved to optimize the microstructure and as a result the magnetic properties, bottom-up approaches exploiting magnetic NPs as building-blocks has emerging as a promising strategy [5, 6]. Indeed, reducing the size down to the nanoscale regime allows the coercivity to be increased, thus leading to an improvement of the performance the permanent magnet. Moreover, the potential magnetic material must fulfil many requirements to guarantee a certain feasibility. In particular, it must display a high spontaneous magnetization, together with a high uniaxial magnetic anisotropy [1, 4].

In this work, the focus is on M-type hexaferrite ( $\text{AFe}_{12}\text{O}_{19}$  where A:  $\text{Sr}^{2+}$ ) NPs, a ferromagnet well-known for their use in a wide range of applications, such as permanent magnets, magnetic recording and data storage materials, components in electrical devices and microwave absorbers [7, 8].  $\text{SrFe}_{12}\text{O}_{19}$  (SFO), thanks to its high Curie temperature ( $T_C \sim 700$  K) [7], chemical stability, high magneto-crystalline anisotropy constant ( $K = 0.35$  MJ  $\text{m}^{-3}$ ), and high magnetic uniaxial anisotropy along the  $c$ -axis [7], is a good candidate to fabricate

nanostructured and/or exchange coupled composites with a greater performance [1, 2]. The magnetic properties of SFO are intrinsically linked to its morpho-structural features, therefore, the size and shape of the crystallites play a crucial role in optimizing their performance [9]. In this context, sol–gel self-combustion synthesis, being a simple, low-cost method, yielding stoichiometric nano-powders [7, 10–13], is a viable approach to synthesize  $\text{SrFe}_{12}\text{O}_{19}$  NPs. Furthermore, it is a powerful method to design bi-phasic nanocomposites (NCs) [14, 15] since it allows tuning the degree of particle agglomeration, and, hence, optimization of the magnetic coupling between the two phases [14, 16]. Hence, this route presents an innovative way to exploit the effect of a matrix, by using one phase as nucleation sites for the second one.

Over the last few years, NCs of complex oxides have emerged as a promising research area because of the number of opportunities that such systems offer regarding their functionalities [17]. Among the various strategies investigated, NCs of exchange-coupled hard and soft magnets have shown promise, allowing the design of new materials with tunable magnetic properties [1, 18]. To achieve high performances, permanent magnets require a strong saturation magnetization ( $M_s$ ) combined with a high coercivity ( $H_c$ ) (large resistance to demagnetization). Despite considerable efforts, few viable materials and alloys have emerged as prototypical compounds, as usually both these values cannot be maximized simultaneously in the same material, in a single hard or soft magnetic phase, as either  $M_s$  or  $H_c$  is low in each case. Hence, a potential strategy is to combine two materials, one with high  $M_s$  and another with large  $H_c$ , on the nanometer scale, to guarantee that they are sufficiently coupled and thus exhibit performances matching or overcoming that of state-of-the art RE-based permanent magnets [1, 19]. However, controlling the coupling between the phases is essential to optimize the magnetic performance. Even if relevant progression has been achieved, many studies have focused exclusively on physically-mixed samples, where the two phases were mechanically ground in appropriate proportions [20], resulting in non-completely exchange coupled systems. In this regard, tailoring the synthesis method can produce prototypical NCs with improved magnetic properties, to approach a novel class of magnets [15, 21, 22].

In this paper, we show that the synthesis conditions of pure nanocrystalline SFO can be optimized to decrease the annealing temperature, without any deterioration in the magnetic performance. Hence, we have investigated the relationship between the structural/morphological features of the nanocrystallites, as well as the effect on the particle agglomeration and shape caused by the synthesis technique, and the resulting magnetic properties. In addition, a first attempt towards the synthesis of SFO-based bi-magnetic NC has been explored,

**Table 1.** List of samples and synthesis details (\* indicates the addition of cetyl trimethylammonium bromide (CTAB)).

Id	Annealing T(°C)	Fe <sup>3+</sup> /Sr <sup>2+</sup> (mol ratio)		Citric acid/total nitrates (mol ratio)
		SFO		
SFO <sub>A</sub>	1000	12		1
SFO <sub>B</sub>	900	10		1
SFO <sub>C</sub> *	800	10		1
Fe <sup>3+</sup> /Co <sup>2+</sup> (mol ratio)				
CFO				
NC	1000	12	2	1
NC <sub>MIX</sub>	—	12	2	1

by coupling the hexaferrite with a soft phase, CoFe<sub>2</sub>O<sub>4</sub> (CFO), whose spinel ferrite structure offers a versatile crystal chemistry, resulting in the possibility to tune the magnetic anisotropy of such systems.

## 2. Synthesis, experimental techniques, and data treatment

### 2.1. Sol–gel technique

**SFO:** The hexagonal strontium ferrites were prepared by a sol–gel combustion process. Briefly, Fe(NO<sub>3</sub>)<sub>3</sub> · 9H<sub>2</sub>O and Sr(NO<sub>3</sub>)<sub>2</sub> · 6H<sub>2</sub>O (Sigma-Aldrich) were dissolved in deionized water in a beaker to give a Fe<sup>3+</sup> concentration of 0.2 M, with an appropriate molar ratio. Then a 1 M citric acid aqueous dispersion was added (molar ratio of total metals to citric acid 1:1). The solution was kept under agitation to dissolve the nitrates at room temperature and NH<sub>3</sub> (30%) (Sigma-Aldrich) was added dropwise to adjust the pH to 7. Next, it was heated on a hot plate to 80 °C to form a gel, thanks to the chelating action of the citric acid. After the entire solution was converted to a dry gel (after ~4 h), the temperature was rapidly increased to 300 °C inducing a flameless self-combustion. The obtained dry powders were ground and annealed at different temperatures (from 600 °C to 1000 °C) with a ramp of 5 °C min<sup>-1</sup> under air, to study the phase evolution. As shown in the electronic supplementary information (ESI, figure S1, available online at [stacks.iop.org/JPD/54/124004/mmedia](https://stacks.iop.org/JPD/54/124004/mmedia)), the investigation on the evolution of the hexaferrite phase formation with thermal treatment allowed us to select three optimal pure samples: SFO<sub>A</sub>, SFO<sub>B</sub>, and SFO<sub>C</sub>, obtained at three different temperatures (1000 °C, 900 °C, and 800 °C), respectively (the synthesis parameters are listed in table 1).

**NC:** The synthesis procedure was adapted to prepare an exchange-coupled hard/soft NC by sol–gel through a simultaneous bi-phasic approach [15, 16]. CFO and SFO precursors, in stoichiometric ratios (as reported in the table 1), were separately dissolved in deionized water in two beakers to give a Fe<sup>3+</sup> concentration of 0.2 M, then a 1 M citric acid aqueous dispersion was added. Subsequently, the dispersions were mixed together and the pH was adjusted to 7. The as-burnt powders were annealed up to 1000 °C to crystallize the

two phases. The amounts of CFO and SFO were chosen such that the weight % of SFO in the NC corresponded to 40% (for comparison, a reference CFO sample was also synthesized and annealed at the same temperature (more details in ESI)).

**NC<sub>MIX</sub>:** A reference sample for the NC was also prepared by physically mixing the two individual components (weight fraction SFO<sub>A</sub>/CFO = 40/60) in a mortar with acetone to obtain a fine mixture of the two powders (NC<sub>MIX</sub>) without any further annealing after mixing. The individual components were chemically synthesized via sol–gel combustion synthesis and treated at 1000 °C: here the phases are SFO<sub>A</sub> and reference CFO.

### 2.2. X-ray powder diffraction (XRPD)

The powder samples were characterized using a Bruker D8 Advance diffractometer (solid state rapid LynxEye detector, Cu Kα radiation, Bragg–Brentano geometry, DIFFRACT plus software) in the 10°–140° 2θ range with a step size of 0.013° (counting time was 8 s per step).

The powder samples were grounded in an agate mortar and suspended in ethanol. A Si substrate was covered with several drops of the resulting suspension, leaving randomly-oriented crystallites after drying. Rietveld analysis was performed on the XRPD data using the FULLPROF program [23]. The diffraction peaks were described by a modified Thompson-Cox-Hastings pseudo-Voigt function. A peak asymmetry correction was made for angles below 40° (2θ). Background intensities were estimated by interpolating between up to 60 selected points. A NIST LaB<sub>6</sub> 660b standard was measured under the same conditions as the samples to account for the instrumental contribution to the peak broadening.

### 2.3. Transmission electron microscopy (TEM)

TEM analysis was carried out using a Philips CM200 microscope operating at 200 kV and equipped with a LaB<sub>6</sub> filament. For TEM observations, the samples, in form of powder, were prepared using the following procedure. A small quantity of powder was dispersed in ethanol and subjected to ultrasonic agitation for approximately one minute. A drop of the suspension was deposited on a commercial TEM grid covered with a thin carbon film. Finally, the grid was kept in air until complete ethanol evaporation.

### 2.4. Magnetic characterization

Magnetic measurements were performed at room temperature using a Quantum Design superconducting quantum interference device magnetometer, which can supply a maximum field of 5 T. To avoid any displacement of the nanopowders during the measurements, the samples were immobilized with a glue in appropriate capsules (no significant magnetic contribution from the glue was observed). Iso-thermal field-dependent magnetization loops were recorded by sweeping the field in the –5 T to +5 T range. To get information about the irreversible processes, direct current demagnetization (DCD) remanence

curves were measured by applying a progressively higher DC reverse field to a sample previously saturated under a field of  $-5$  T and by recording, for each step, the value of remanence that was then plotted as a function of the reverse field [24]. All the measurements were corrected by including the demagnetizing factor for packed particles ( $N_p$ ) considering a dense system  $\varphi \sim 0.3$  and a spherical shape for particles (more details are reported in ESI) [25]. To evaluate the maximum energy product  $(BH)_{MAX}$ , providing a useful figure of merit of permanent magnet performance [26], the theoretical density of SFO was used [27].

### 2.5. Composition analysis

Energy dispersive spectrometry (EDS) measurements were performed using a Tescan Vega3 scanning electron microscope equipped with an EDAX Element microanalysis. The atomic concentrations of Sr, Fe, and Co were measured on three different large areas of the sample (each area was approximately  $1-2 \times 10^4 \mu\text{m}^2$ ). For analysis, the samples were simply attached to an aluminium stub by a self-adhesive carbon disc (no conductive coating was used).

## 3. Results and discussion

### 3.1. Tuning single-phase systems via the structure/morphology

The phase evolution of  $\text{SrFe}_{12}\text{O}_{19}$  as a function of the thermal treatment (figure S1) clearly reveals that an annealing temperature of  $1000^\circ\text{C}$  is necessary to obtain a single phase ( $\text{SFO}_A$ ). However, by optimizing the synthesis procedure, the threshold value has been first decreased to  $900^\circ\text{C}$  ( $\text{SFO}_B$ ) by adjusting the molar ratio between  $\text{Fe}^{3+}$  and  $\text{Sr}^{2+}$  from 12 to 10 [13, 28], and then, further to  $800^\circ\text{C}$  with the addition of a surfactant while keeping the molar ratio at 10 ( $\text{SFO}_C$ ) [29], where the recurrent formation of antiferromagnetic hematite as secondary phase is not detected. The elemental analysis performed by EDS has confirmed the correct stoichiometry for all the samples.

As an example, the XRPD pattern for  $\text{SFO}_A$  is reported in figure 1(a): the data show a single-phase behaviour and all the reflections can be ascribed to the hexagonal structure typical of strontium hexaferrite, with space group  $P63/mmc$  [30]. Reflections due to secondary phases and impurities are not detected. The unit cell parameters have been extracted using Rietveld refinement [31]. The values, reported in table 2, show a good agreement with the [30] for the M-type SFO, with slight variations, presumably due to the different synthesis conditions.

On the basis of TEM analysis (reported later on), assuming strain-free anisotropic platelets, the crystallite sizes have been obtained adopting the vector-size model in FULLPROF, considering the platelet's normal along the crystallographic  $c$ -axis (001). As shown in the detail of XRPD patterns (figure 1(b)), it is noticeable that the Bragg peak ascribed to the 004 reflection show a wide broadening, that decreases for higher annealing temperature. The size extracted along the  $ab$ -plane and along

the  $c$ -axis are referred to as  $d_{ab}$  and  $d_c$ , respectively. In addition to this, a March-Dollase model has been used taking into consideration a preferred orientation along the (001)-Bragg direction, to evaluate the platelet-like orientation of the ferrites. From the analysis of peak broadening in the previous patterns, it is clear that there is a dependence of the size on the thermal treatment, since the broadening becomes smaller when the temperature is increased: the  $ab$  and  $c$  sizes increase from  $\sim 74$  to  $\sim 149$  nm and from  $\sim 52$  to  $\sim 134$  nm, respectively, when the annealing temperature is enhanced from  $800^\circ\text{C}$  to  $1000^\circ\text{C}$ , as reported in table 2. By calculating the aspect ratio ( $R = d_{ab}/d_c$ ), it appears that the nanocrystallites are almost isotropic:  $\text{SFO}_B$  and  $\text{SFO}_C$  show  $R$ -values typical of  $\text{SrFe}_{12}\text{O}_{19}$  obtained by a sol-gel approach [13]; besides, the higher the annealing temperature, the more isotropic are the crystallites. All the refined patterns are included in the ESI, together with the corresponding parameters and fit quality factors (figure S3 and tables S1-S3).

As a last step of refinement, a CIF file has been generated from  $\text{SFO}_A$ , to visualize the single unit cell (figure 1(d)) using VESTA [32] and thus to describe the complex crystalline structure of this compound, which is at the origin of the resulting magnetic structure [7]. The M-type structure is made up of alternating spinel ( $\text{Fe}_6\text{O}_8^{2+}$ ) and hexagonal sub-structures ( $\text{SrFe}_6\text{O}_{11}^{2-}$ ) where the  $\text{O}^{2-}$  ions are organized as hexagonal close-packed (hcp) layers, with the substitution of  $\text{Sr}^{2+}$  for an  $\text{O}^{2-}$  in the hexagonal layer.  $\text{Fe}^{3+}$  ions are distributed in five different interstitial crystallographic sites deriving from the packing of oxygen ions: three in the octahedral sites (2a, 12k, and 4f2), one in the tetrahedral site (4f1), and one in the trigonal bipyramidal site (2b). The replacement of atoms of oxygen with a large divalent metal ion causes a disturbance in the lattice because of the size differences, and is responsible for the high magneto-crystalline anisotropy [2, 7]. Thus, considering the various types of coupling between iron ions in different sites, the resulting coupling of the moments between the blocks is ferromagnetic.

TEM analysis (figure 2) reveals that samples are composed of irregular platelets interconnected to form a porous mosaic. The platelet size increases as the annealing temperature is raised. In particular, the lateral dimensions of the platelets range from 50 to 1000 nm, from 20 to 160 nm, and from 10 to 140 nm for  $\text{SFO}_A$ ,  $\text{SFO}_B$ , and  $\text{SFO}_C$ , respectively. It must be stressed that crystallites' sizes obtained by XRPD measurements are quite lower than platelet dimensions, suggesting a polycrystalline nature of the single platelets. In addition, the extracted circularity ( $C$ ), which describes the morphology of the particles [33, 34], is equal to 0.84(2) for  $\text{SFO}_B$  and  $\text{SFO}_C$ , this value being typical of hexagonal shapes, while a slight deviation is observed for  $\text{SFO}_A$  ( $C = 0.82(2)$ ), probably because of a higher degree of sintering owing to a higher annealing temperature. Typical TEM selected area electron diffraction (SAED) patterns of the samples are shown in the insets of figure 2. They are composed of more or less continuous rings revealing the polycrystalline nature of the samples. Furthermore, being obtained with the same microscope aperture, the continuity of the diffraction rings can be related to the different dimensions of the grains: smaller for  $\text{SFO}_C$  (almost

**Table 2.** Lattice parameters ( $a$ ,  $b$ , and  $c$ ), apparent sizes ( $d_{ab}$  and  $d_c$ ), and platelet-ratio ( $R$ ) extracted from Rietveld refinement (left); Saturation magnetizations ( $M_S$ ), reduced remanence magnetization  $M_R/M_S$ , coercive field ( $H_C$ ) and average switching field ( $H_{SW}$ ) measured at 300 K (right) (Uncertainties in the last digit are given in parenthesis).

Id	$a = b$ (Å)	$c$ (Å)	$d_{ab}$ (nm)	$d_c$ (nm)	$R$ : $d_{ab}/d_c$	$M_S$ (Am <sup>2</sup> kg <sup>-1</sup> )	$M_R/M_S$	$H_C$ (kA m <sup>-1</sup> )	$H_{SW}$ (kA m <sup>-1</sup> )
SFO <sub>A</sub>	5.87948(1)	23.04942(3)	149(5)	134(3)	1.11	67.3(5)	0.49	469(3)	533(2)
SFO <sub>B</sub>	5.87938(1)	23.05334(6)	89(7)	68(5)	1.30	64.9(3)	0.50	480(2)	530(1)
SFO <sub>C</sub>	5.88065(1)	23.04869(11)	74(6)	52(2)	1.42	63.6(7)	0.50	468(2)	536(2)

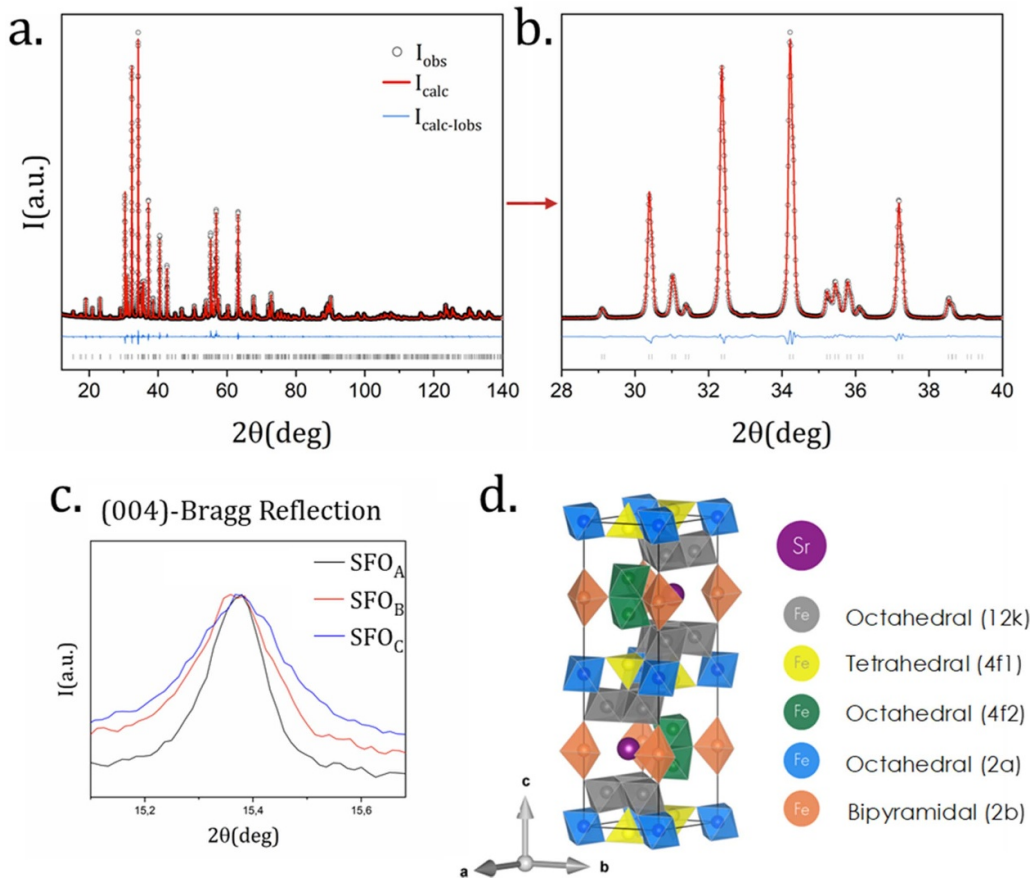


**Figure 1.** (a) XRPD pattern, including Rietveld refinement for SFO<sub>A</sub>; (b) detail of SFO<sub>A</sub> to show the purity of the pattern; (c) peak broadening for SFO<sub>A</sub>, SFO<sub>B</sub>, and SFO<sub>C</sub>; (d): unit cell of SFO<sub>A</sub> obtained using VESTA.

continuous diffraction rings), larger for SFO<sub>A</sub> (discontinuous diffraction rings). All the lattice interplanar distances obtained by analysing SAED patterns can be associated to the SFO phase; no other phases have been detected.

In figures 3(a)–(c), isothermal (300 K) field-dependent magnetization loops of SFO<sub>A</sub>, SFO<sub>B</sub>, and SFO<sub>C</sub> are shown. The magnetic behaviour looks very similar for all the samples and the extracted magnetic parameters are reported in table 1. Regarding the coercive field, the highest value is found for SFO<sub>B</sub>; it marginally increases up to 480(2) kA m<sup>-1</sup>, 3% more compared to that of SFO<sub>C</sub>. This is generally associated to a correspondingly larger value of  $d_c$ , as it is parallel to the easy magnetization axis of the ferrite, thus affecting the shape anisotropy [5, 35]. On the other hand, it is noteworthy that the coercive field decreases down to 469(3) kA m<sup>-1</sup> for the sample SFO<sub>A</sub>. Considering that  $H_c$  should increase with  $d_c$ , the same trend should be expected; however, after excluding

the possibility of being close to the critical volume for a single domain particle [29, 30] and the presence of amorphous material (i.e. the sample is well crystallized), the decrease in  $H_C$  can be ascribed to a huge change in the morphology/volume of the particles [31, 32], owing to the very high annealing temperature. Further studies are necessary to confirm this, nevertheless, our hypothesis is supported by the fact that the coercivity drops down to 376 kA m<sup>-1</sup> when the annealing temperature for SFO<sub>A</sub> is further increased to 1100 °C (figure S4), confirming the necessity to keep the thermal conditions as low as possible in order to guarantee optimal conditions. To get further insight into the reversal process of the magnetization, DCD experiments were performed (figures 3(a)–(c)). The curves were differentiated to evaluate the trend of the irreversible susceptibility ( $\chi_{irr}$ ) as a function of the reverse field (figure 3(d)) This quantity measures the energy barrier distribution, which is associated to the distribution of the particles' switching field

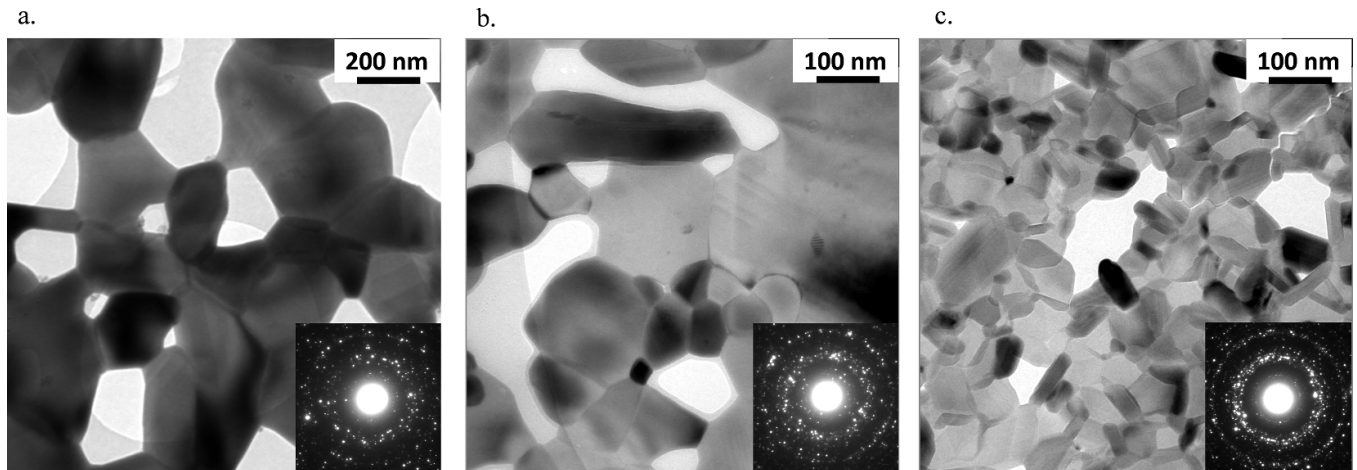


**Figure 2.** TEM images of the hexaferrites are shown in panels (a) SFO<sub>A</sub>, (b) SFO<sub>B</sub> and (c) SFO<sub>C</sub>. The SAED patterns are reported in insets of the respective figures.

(SFD), defined as the field  $H_{SW}$  necessary to overcome the energy barrier during an irreversible reversal process [36]. The three samples present similar SFDs centred at a field  $H_{SW}$  that changes marginally from 530 to 536 kA m<sup>-1</sup>. The difference between  $H_{SW}$  and  $H_C$  measures the degree of reversible processes, which is higher for samples SFO<sub>A</sub> and SFO<sub>C</sub>, thus explaining the reduced value of  $H_C$  in such samples.

In view of the fact that our purpose is to employ SFO as a matrix to design biphasic magnetic NCs to be used as permanent magnets, its suitability was investigated by calculating the  $(BH)_{MAX}$  (see details of estimation in ESI, figure S5). SFO<sub>A</sub>, SFO<sub>B</sub>, and SFO<sub>C</sub> exhibit similar performance, with  $(BH)_{MAX}$  values of 8.9, 8.4, and 7.9 kJ m<sup>-3</sup>, respectively. These results are in agreement with previously reported values obtained by similar synthesis approaches [13, 37]. This study allowed us to establish, on the basis of the energy product, the potentiality of hexaferrite NPs for the realization of RE free permanent magnets, showing that the different synthesis conditions (i.e. decreasing the annealing temperature) do not considerably affect it.

### 3.2. Sol-gel synthesized NC—tuning bi-phasic systems via composition/interphase coupling interaction

Sol-gel synthesis has been revealed to be a reliable approach to obtain bi-magnetic NCs with homogeneous dispersion of the constituent phases [14–16, 21, 22]. Here, the method was adapted to couple two different magnetic phases to develop improved magnetic NCs, consisting of a hard SFO phase magnetically coupled to a softer CFO phase, the latter having a higher value of saturation magnetization (0.45 MA m<sup>-1</sup>) than SFO (0.38 MA m<sup>-1</sup>). From XRPD characterization, there is evidence of the crystallization of a spinel phase ascribed to CFO, already after the auto-combustion (as shown in figure S2), in presence of the hexagonal ferrite precursors. By following the phases' evolution in a wide temperature range, pure SFO appears at 1000 °C. As reported in figure 4(a), the pattern clearly contains the two phases, well resolved and without impurities.

Rietveld analysis was performed by modelling the SFO as a hexagonal phase (P63/mmc 194) and the CFO as a spinel (Fd-3 m 227) [38]. The site occupancies of the atoms were not refined given that Co and Fe are not distinguishable by x-ray diffraction. The stoichiometry of both the compounds was checked by EDS, confirming the expected composition. The extracted lattice parameters are  $a = b = 5.88155(2)$  Å and  $c = 23.02613(17)$  Å for SFO, and  $a = b = c = 8.37976(1)$  Å for CFO. Since the values for both phases are in a very good agreement with the reference values [30, 39], and no peak shift for either phase is observed in the pattern, we can reasonably assume that the two phases are well crystallized, without undergoing any evident diffusion. This hypothesis is also supported by the fact that the obtained x-ray densities for each phase are in perfect agreement with the theoretical ones [27], evidence of a resulting overall good dispersion, and, furthermore, the estimated weight percentages are close to the nominal ones (40 SFO/60 CFO w/w %). The sizes obtained in the refinements (whose details are reported in ESI) clearly demonstrate an evident effect of the synthesis route. Indeed, compared to CFO annealed at 1000 °C (ESI), the average crystallite size dramatically decreases from 210 (34) nm to 67(5) nm. Interestingly, at the same time, the SFO undergoes an impactful effect as  $d_c$  drops from ~134 to 45(6) nm and  $d_{ab}$  from ~149 to 70(2), resulting in an aspect ratio  $R = 1.55$ . We can conclude that the as-synthesized cobalt ferrite acts as a template, around which the growth of the hexaferrite takes place, each phase restricting the growth of the other, in a symbiotic way as already observed before [15, 16].

A typical TEM bright field image of the SFO/CFO NC is shown in figure 4(b) with the corresponding SAED pattern (inset). The sample can be again described as formed by irregular platelets interconnected to form a porous mosaic. From the image, it is not possible to distinguish the SFO and CFO grains, and even the TEM dark field technique is not suitable to evidence the two phases because the lattice interplanar distances are very similar, thus making it impossible to select diffraction spots coming only from one of the two phases. The

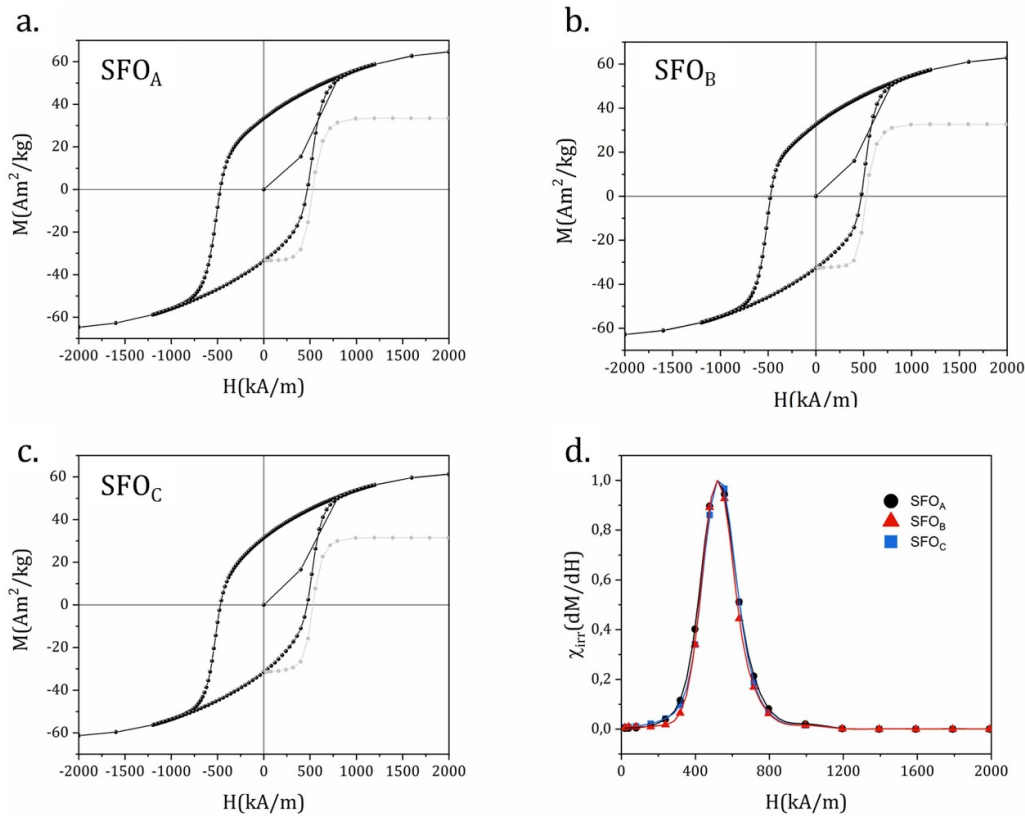


**Figure 3.** Magnetization  $M$  vs. magnetic field  $H$  curve (black filled dots) and  $M_{DCD}$  vs. reverse magnetic field (grey filled dots) of (a) SFO<sub>A</sub>, (b) SFO<sub>B</sub>, and (c) SFO<sub>C</sub>, (d) normalized switching field distributions (SFD) as obtained from the first order derivatives of the corresponding  $M_{DCD}$  curves at 300 K.

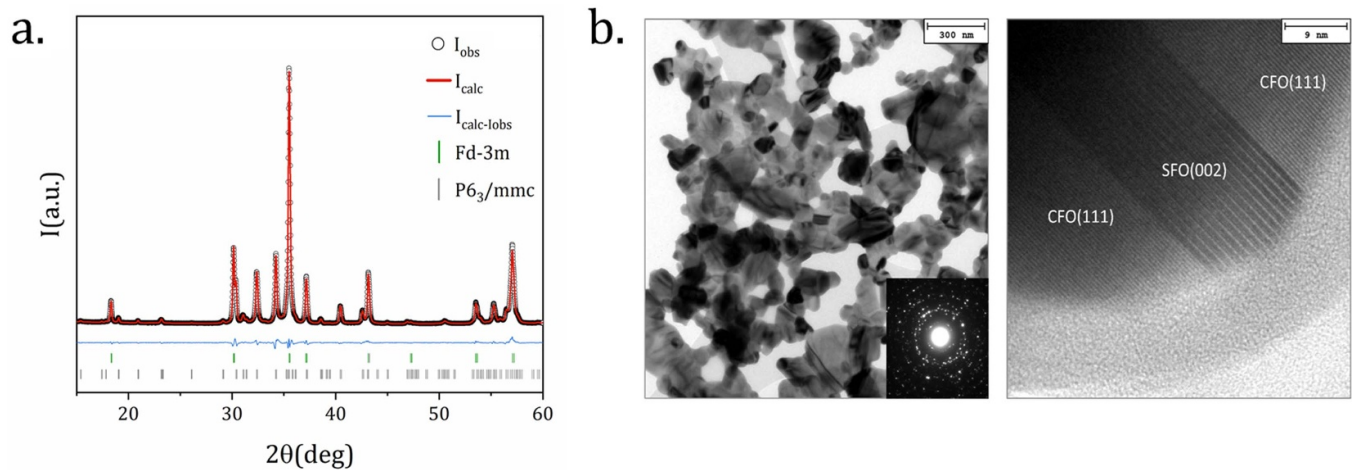


**Figure 4.** (a) XRPD pattern, including Rietveld refinement for SFO/CFO NC; (b) TEM bright field image of NC (left panel) with the SAED pattern corresponding to the sample area imaged (inset), and high resolution (HR) TEM image (right panel) highlighting the presence and distribution of SFO and CFO nanocrystals in NC.

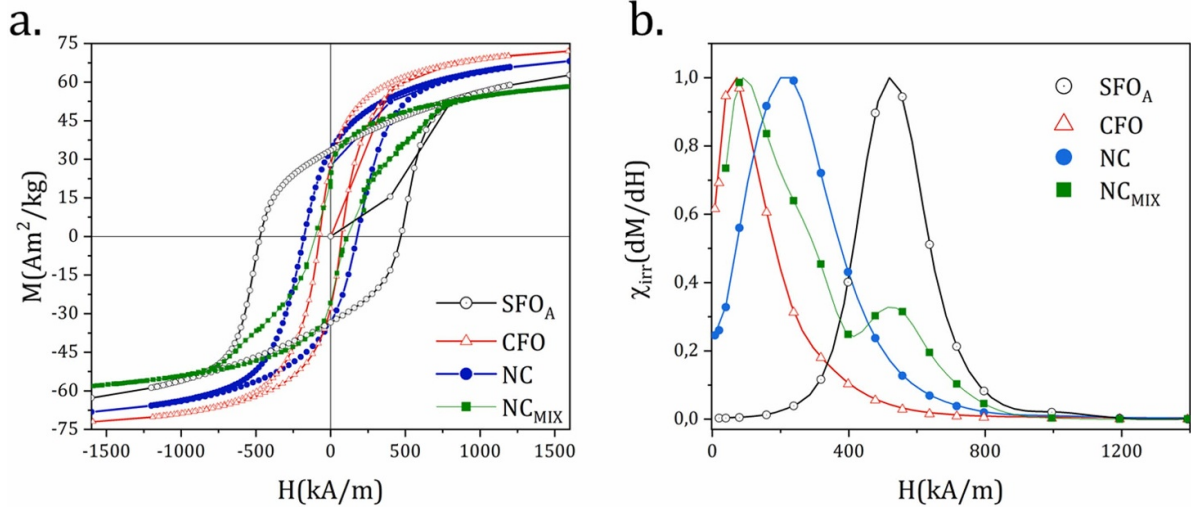
only way to recognize SFO and CFO grains is to use high resolution (HR) TEM images. In particular, figure 4(b) shows an SFO grain surrounded by two CFO nanocrystals. Analysing the fast Fourier transform of the atomic resolved image, it was possible to unambiguously identify the grains. It is important to stress that the SFO nanocrystals appear confined among the CFO ones, with SFO (002) planes parallel to the CFO (111)

planes. This image clearly suggests an oriented growth of the two phases, with the SFO hexagonal basal plane parallel to the CFO (111) planes which have a hexagonal symmetry, thus confirming the previous XRPD data interpretation of a symbiotic growth between the two phases.

To clarify the relationship between the morphological-structural features and magnetic coupling, field-dependent

**Table 3.** Mean sizes ( $d$ ) extracted from refinement, saturation moment ( $M_S$ ), reduced remanence magnetization  $M_R/M_S$ , coercive field ( $H_C$ ), and average switching field ( $H_{SW}$ ) measured at 300 K (Uncertainties in the last digit are given in parenthesis).

Id	$d_{ab}^{\text{SFO}}$ (nm)	$d_c^{\text{SFO}}$ (nm)	$\langle d \rangle^{\text{CFO}}$ (nm)	$M_S$ ( $\text{Am}^2 \text{kg}^{-1}$ )	$M_R/M_S$	$H_C$ ( $\text{kA m}^{-1}$ )	$H_{SW}$ ( $\text{kA m}^{-1}$ )
SFO <sub>A</sub>	149(5)	134(3)		67.3(5)	0.49	469(3)	533(2)
CFO			210(34)	75.2(7)	0.37	74(4)	71(5)
NC	70(7)	45(6)	67(5)	71.7(4)	0.46	177(6)	250(2)

**Figure 5.** (a) Magnetization  $M$  vs. magnetic field  $H$  curve and (b) normalized switching field distributions (SFD) of SFO<sub>A</sub>, CFO, NC and NC<sub>MIX</sub> at 300 K.

magnetization loops for NC, SFO<sub>A</sub> (previously shown in figure 3) and CFO are reported in figure 5(a). All the curves exhibit a single reversal process of magnetization, suggesting that the two magnetic phases are homogeneously dispersed and strongly coupled, owing to the efficiency of the one-pot sol-gel method. As a reference sample, the magnetization curve of NC<sub>MIX</sub> prepared by physically mixing the starting precursors' phases is also reported, showing a bimodal hysteresis loop, typical of weakly coupled systems. The NC shows an intermediate magnetic behaviour between the two phases, as proved by the comparison of the parameters reported in table 3. Both the  $M_S$  and  $M_R/M_S$  values increase with respect to the corresponding values of SFO, suggesting a good degree of magnetic coupling between the phases. In addition, the  $H_C$  value is consistently decreased in the composite with respect to that of SFO, as a result of the large amount of soft phase (60 w/w %). However, the magnetic performance of NC results perfectly within the limit of exchange-coupling, as its  $H_C$  is in agreement with the calculated value ( $187 \text{ kA m}^{-1}$ ), according to the following equation  $H_C = H_H (1 - f)$  by considering the coercivity of the hard phase  $H_H = 469 \text{ kA m}^{-1}$  (for SFO<sub>A</sub>) and the volume fraction of the soft one  $f = 0.6$  [40]. While designing NCs suitable for various applications, it is fundamental to carefully control the size and distribution of the soft/hard-phase regions, to limit the deterioration of the desired magnetic performance. In this regard, it is noteworthy that generally the coercive field of CFO increases with a decrease in the particle size (as illustrated in figure S4 for single-phase CFO) [41]. Hence, the symbiotic growth

of the NC, where the presence of one phase prevents grain growth of the other phase, thus leading to a smaller crystallite size of the soft CFO actually proves to be a beneficial effect with regard to the decrease in  $H_C$  compared to that of SFO. As a matter of fact, the normalized  $\chi_{irr}$  plot for the NC (in figure 5(b)) clearly shows a single reversal process of magnetization with CFO and SFO phases strongly coupled, with an intermediate  $H_{SW}$  value compared to that of the CFO and SFO single phases, thus, proving the efficiency of controlling the size and distribution of hard/soft-phase regions thanks to the synthesis method. In contrast, the DCD curve of NC<sub>MIX</sub> presents two strong contributions, centred at different fields that can be attributed to the reversal processes of the two individual phases (SFO and CFO), without any sign of coupling.

In brief, magnetic measurements reveal significant differences in magnetic coupling in the two samples (NC and NC<sub>MIX</sub>). We have demonstrated that these differences are related to the differences in synthesis technique, specifically, the symbiotic effect of the matrix that opens up the way for regulating the degree of tunability through the design of the NCs.

#### 4. Conclusion

We have shown that sol-gel self-combustion synthesis is an efficient and reproducible approach to synthesize SFO nanocrystals. By optimizing the synthesis conditions, we were

able to decrease the annealing temperature, allowing us to investigate the effect of different thermal treatments to vary the size of the nanocrystallites. The obtained NPs are almost isotropic, with a platelet-like shape. Through XRPD, TEM, and magnetic measurements, we showed a significant relation between the morphology (i.e. size and shape), and resulting magnetic properties of the hexagonal ferrite, which show a clear dependence on the platelet size along the c-axis. In particular, the evaluation of the magnetic performance for permanent magnet applications shows similar values in all the samples, thereby demonstrating the feasibility of reducing the annealing temperature without any deterioration in the physical properties.

We have also explored the use of SFO in bi-magnetic NCs, by coupling it with a well-known soft magnet, CFO. The attempt not only shows the feasibility of the sol-gel approach in synthesizing such NCs, but also the tunability of the magnetic anisotropy that can be achieved by chemical engineering, by tuning the effect of confinement during the growth of both phases.

## Acknowledgments

We thank the Swedish Energy Agency and Swedish Research Council (VR) for financially supporting this work. T Sarkar acknowledges financial support from VR (starting Grant No. 2017-05030).

## ORCID iDs

Pierfrancesco Maltoni  <https://orcid.org/0000-0001-9834-3164>

Tapati Sarkar  <https://orcid.org/0000-0003-4754-2504>

Gaspard Varvaro  <https://orcid.org/0000-0001-7313-7268>

Gianni Barucca  <https://orcid.org/0000-0002-7368-6264>

Davide Peddis  <https://orcid.org/0000-0003-0810-8860>

Roland Mathieu  <https://orcid.org/0000-0002-5261-2047>

## References

- [1] Balamurugan B, Sellmyer D J, Hadjipanayis G C and Skomski R 2012 Prospects for nanoparticle-based permanent magnets *Scr. Mater.* **67** 542–7
- [2] Lewis L H and Jiménez-Villacorta F 2013 Perspectives on permanent magnetic materials for energy conversion and power generation *Metall. Mater. Trans. A* **44** 2–20
- [3] Skokov K P and Gutfleisch O 2018 Heavy rare earth free, free rare earth and rare earth free magnets—vision and reality *Scr. Mater.* **154** 289–94
- [4] Coey J M D 2012 Permanent magnets: plugging the gap *Scr. Mater.* **67** 524–9
- [5] Saura-Múzquiz M, Granados-Miralles C, Andersen H L, Stingaciu M, Avdeev M and Christensen M 2018 Nanoengineered high-performance hexaferrite magnets by morphology-induced alignment of tailored nanoplatelets *ACS Appl. Nano Mater.* **1** 6938–49
- [6] Yue M, Zhang X and Liu J P 2017 Fabrication of bulk nanostructured permanent magnets with high energy density: challenges and approaches *Nanoscale* **9** 3674–97
- [7] Pullar R C 2012 Hexagonal ferrites: a review of the synthesis, properties and applications of hexaferrite ceramics *Prog. Mater. Sci.* **57** 1191–334
- [8] Chakradhary V K and Akhtar M J 2017 Microwave absorption properties of strontium ferrite and carbon black based nanocomposites for stealth applications *2017 IEEE Asia Pacific Microwave Conf. (APMC) (IEEE)* pp 678–81
- [9] Saura-Múzquiz M, Eikeland A Z, Stingaciu M, Andersen H L, Granados-Miralles C, Avdeev M, Luzin V and Christensen M 2020 Elucidating the relationship between nanoparticle morphology, nuclear/magnetic texture and magnetic performance of sintered SrFe<sub>12</sub>O<sub>19</sub> magnets *Nanoscale* **12** 9481–94
- [10] Cannas C, Ardu A, Niznansky D, Peddis D, Piccaluga G and Musinu A 2011 Simple and fast preparation of pure maghemite nanopowders through sol-gel self-combustion *J. Sol-Gel Sci. Technol.* **60** 266–74
- [11] Das A, Roychowdhury A, Pati S P, Bandyopadhyay S and Das D 2015 Structural, magnetic and hyperfine properties of single-phase SrFe<sub>12</sub>O<sub>19</sub> nanoparticles prepared by a sol-gel route *Phys. Scr.* **90** 025802
- [12] Zhuravlev V A, Minin R M, Itin V I, Politov M V, Yu Lilenko I and Ufimtsev M R 2017 Structure parameters and magnetic properties of nanosized strontium hexaferrite prepared by the sol-gel combustion method *IOP Conf. Ser.: Mater. Sci. Eng.* **168** 012075
- [13] Eikeland A Z, Stingaciu M, Mamakhel A H, Saura-Múzquiz M and Christensen M 2018 Enhancement of magnetic properties through morphology control of SrFe<sub>12</sub>O<sub>19</sub> nanocrystallites *Sci. Rep.* **8** 7325
- [14] Muscas G, Anil Kumar P, Barucca G, Concas G, Varvaro G, Mathieu R and Peddis D 2016 Designing new ferrite/manganite nanocomposites *Nanoscale* **8** 2081–9
- [15] Sayed F, Kotnana G, Muscas G, Locardi F, Comite A, Varvaro G, Peddis D, Barucca G, Mathieu R and Sarkar T 2020 Symbiotic, low-temperature, and scalable synthesis of bi-magnetic complex oxide nanocomposites *Nanoscale Adv.* **2** 851–9
- [16] Sayed F, Muscas G, Jovanovic S, Barucca G, Locardi F, Varvaro G, Peddis D, Mathieu R and Sarkar T 2019 Controlling magnetic coupling in bi-magnetic nanocomposites *Nanoscale* **11** 14256–65
- [17] Chen A, Su Q, Han H, Enriquez E and Jia Q 2019 Metal oxide nanocomposites: a perspective from strain, defect, and interface *Adv. Mater.* **31** 1803241
- [18] Zeng H, Li J, Liu J P, Wang Z L and Sun S 2002 Exchange-coupled nanocomposite magnets by nanoparticle self-assembly *Nature* **420** 395–8
- [19] Sellmyer D J, Balamurugan B, Das B, Mukherjee P, Skomski R and Hadjipanayis G C 2015 Novel structures and physics of nanomagnets (invited) *J. Appl. Phys.* **117** 172609
- [20] Ateia E E, Abdelamksoud M K and Rizk M A 2017 Improvement of the physical properties of novel (1-x) CoFe<sub>2</sub>O<sub>4</sub> + (x) LaFeO<sub>3</sub> nanocomposites for technological applications *J. Mater. Sci. Mater. Electron.* **28** 16547–53
- [21] Kotnana G, Sayed F, Joshi D C, Barucca G, Peddis D, Mathieu R and Sarkar T 2020 Novel mixed precursor approach to prepare multiferroic nanocomposites with enhanced interfacial coupling *J. Magn. Magn. Mater.* **511** 166792
- [22] Sarkar T, Muscas G, Barucca G, Locardi F, Varvaro G, Peddis D and Mathieu R 2018 Tunable single-phase magnetic behavior in chemically synthesized AFeO<sub>3</sub>—MFe<sub>2</sub>O<sub>4</sub> (A = Bi or La, M = Co or Ni) nanocomposites *Nanoscale* **10** 22990–3000
- [23] Rodríguez-Carvajal J 1993 Recent advances in magnetic structure determination by neutron powder diffraction *Phys. B: Condens. Matter.* **192** 55–69
- [24] Peddis D, Jönsson P E, Laureti S and Varvaro G 2014 Magnetic interactions: a tool to modify the magnetic

- properties of materials based on nanoparticles *Frontiers of Nanoscience* vol 6, ed C Binns (Amsterdam: Elsevier)
- [25] Normile P S, Andersson M S, Mathieu R, Lee S S, Singh G and De Toro J A 2016 Demagnetization effects in dense nanoparticle assemblies *Appl. Phys. Lett.* **109** 152404
- [26] López-Ortega A, Lottini E, Fernández C D J and Sangregorio C 2015 Exploring the magnetic properties of cobalt-ferrite nanoparticles for the development of a rare-earth-free permanent magnet *Chem. Mater.* **27** 4048–56
- [27] Jenuš P, Topole M, McGuinness P, Granados-Miralles C, Stingaciu M, Christensen M, Kobe S and Žužek Rožman K 2016 Ferrite-based exchange-coupled hard-soft magnets fabricated by spark plasma sintering ed A Belik *J. Am. Ceram. Soc.* **99** 1927–34
- [28] Nga T T V, Duong N P, Loan T T and Hien T D 2014 Key step in the synthesis of ultrafine strontium ferrite powders (SrFe<sub>12</sub>O<sub>19</sub>) by sol–gel method *J. Alloys Compd.* **610** 630–4
- [29] Hari Krishnan V, Saravanan P, Ezhil Vizhi R, Babu D R, Vinod V T P, Kejzlar P and Černík M 2016 Effect of annealing temperature on the structural and magnetic properties of CTAB-capped SrFe<sub>12</sub>O<sub>19</sub> platelets *J. Magn. Mater.* **401** 775–83
- [30] Obradors X, Solans X, Collomb A, Samaras D, Rodriguez J, Pernet M and Font-Altaba M 1988 Crystal structure of strontium hexaferrite SrFe<sub>12</sub>O<sub>19</sub> *J. Solid State Chem.* **72** 218–24
- [31] McCusker L B, Von Dreele R B, Cox D E, Louër D and Scardi P 1999 Rietveld refinement guidelines *J. Appl. Crystallogr.* **32** 36–50
- [32] Momma K and Izumi F 2008 VESTA : a three-dimensional visualization system for electronic and structural analysis *J. Appl. Crystallogr.* **41** 653–8
- [33] Stevenson A P, Blanco Bea D, Civit S, Antoranz Contera S, Iglesias Cerveto A and Trigueros S 2012 Three strategies to stabilise nearly monodispersed silver nanoparticles in aqueous solution *Nanoscale Res. Lett.* **7** 151
- [34] Römer I, Gavin A J, White T A, Merrifield R C, Chipman J K, Viant M R and Lead J R 2013 The critical importance of defined media conditions in *Daphnia magna* nanotoxicity studies *Toxicol. Lett.* **223** 103–8
- [35] Gjørup F H, Saura-Múzquiz M, Ahlburg J V, Andersen H L and Christensen M 2018 Coercivity enhancement of strontium hexaferrite nano-crystallites through morphology controlled annealing *Materialia* **4** 203–10
- [36] Laureti S, Varvaro G, Testa A M, Fiorani D, Agostinelli E, Piccaluga G, Musinu A, Ardu A and Peddis D 2010 Magnetic interactions in silica coated nanoporous assemblies of CoFe<sub>2</sub>O<sub>4</sub> nanoparticles with cubic magnetic anisotropy *Nanotechnology* **21** 315701
- [37] Mohseni F, Pullar R C, Vieira J M and Amaral J S 2019 Enhancement of maximum energy product in exchange-coupled BaFe<sub>12</sub>O<sub>19</sub>/Fe<sub>3</sub>O<sub>4</sub> core-shell-like nanocomposites *J. Alloys Compd.* **806** 120–6
- [38] Granados-Miralles C, Quesada A, Saura-Múzquiz M, Andersen H L, Fernández J F and Christensen M 2020 Expanding the tunability and applicability of exchange-coupled/decoupled magnetic nanocomposites *Mater. Chem. Front.* **4** 1222–30
- [39] Popescu M and Ghizdeanu C 1979 Cation distribution in cobalt ferrite-aluminates *Phys. Status Solidi* **52** K169–72
- [40] Skomski R, Manchanda P, Kumar P K, Balamurugan B, Kashyap A and Sellmyer D J 2013 Predicting the future of permanent-magnet materials *IEEE Trans. Magn.* **49** 3215–20
- [41] Fullerton E E, Jiang J and Bader S 1999 Hard/soft magnetic heterostructures: model exchange-spring magnets *J. Magn. Mater.* **200** 392–404